Pergamon

Journal of Atmospheric and Solar-Terrestrial Physics, Vol. 59, No. 13, pp. 1587–1599, 1997

PII: S0021-9169(96)00158-4
1364-6826/97 $17.00+0.00

Imaging science contributions to equatorial aeronomy: initial results from the MISETA program

Michael Mendillo,* Jeffrey Baumgardner, Marlene Colerico and Daniel Nottingham
Center for Space Physics, Boston University, Boston, U.S.A.

(*Received* 11 *December* 1995; *accepted* 9 *September* 1996)

Abstract—Optical diagnostic techniques have been applied to studies of equatorial aeronomy for nearly half a century. The use of scanning photometers and two-dimensional imagers to observe the spatial patterns associated with low-latitude emissions has been an increasingly used approach during the last few decades. In this paper we review the rationale for the use of all-sky cameras at equatorial latitudes, with particular emphasis on the quantitative information about structures and dynamics that can be extracted from airglow images. The new imaging science instrument at Arequipa, Peru, constructed for the MISETA Program is used as a case study for such techniques. Results derived include: (a) occurrence patterns of several emission features, (b) onset and growth characteristics of airglow depletions associated with equatorial spread-*F*, (c) zonal plasma drifts and their altitude dependence, (d) gravity waves in the mesosphere, and (e) transient optical signatures of thermospheric dynamics associated with the midnight temperature maximum at low latitudes. © 1997 Elsevier Science Ltd

INTRODUCTION

As part of the U.S. NSF CEDAR Program of upper atmospheric research, Multi-Instrumented Studies of Equatorial Thermospheric Aeronomy (MISETA) commenced in October 1993 at several sites in Peru. Figure 1 shows the locations of these instruments: an incoherent scatter radar (ISR) and ionosonde in Jicamarca are operated by Cornell University and the University of Lowell, respectively; a spaced receiver system at Ancon is operated jointly by Boston College and the Air Force Phillips Laboratory, with a Fabry–Perot Interferometer and an all-sky airglow imaging camera being operated by Clemson University and Boston University, respectively, in Arequipa. Here, we report on the first 18 months of observations of the imaging science component of the MISETA Program to illustrate the many aspects of equatorial aeronomy that can be investigated using wide angle airglow imaging techniques.

Imaging science contributes to atmospheric research in two fundamental ways. First, and consistent with the defining goals of the MISETA initiative, an all-sky camera system provides geophysical context for all other line-of-site diagnostics. These include radio and radar observations of plasma characteristics along specific ray paths, multi-point FPI observations of thermospheric winds and temperatures, and for occasional in-situ samplings of ionospheric parameters via satellite overflights or during sounding rocket campaigns. The second area of contribution is independent optical aeronomy, i.e., in

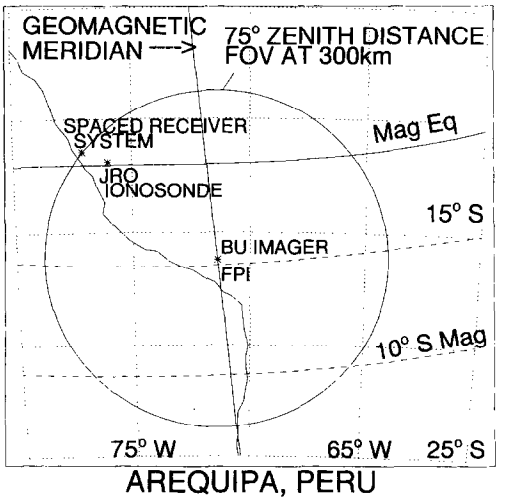

Fig. 1. A map of the Peruvian sector showing the location of instruments that contribute to the MISETA program. The all-sky imaging located in Arequipa has a field of view (FOV) of 180°, with easily usable data spanning ±75° of zenith distance. The projection of this 150° FOV at the typical airglow height of 300 km for 6300 Å is shown.

*Author to whom correspondence should be sent.

the results that flow from analysis of patrol mode images taken over long time periods when other diagnostics may or may not be in operation.

At an equatorial site, the areas of study derived from images include:

1. morphology patterns over space and time of various emissions over diurnal, seasonal and yearly scales.
2. Onset and growth patterns of airglow depletions associated with equatorial spread-*F* (ESF) instabilities.
3. *F*-region zonal plasma drifts derived from the motion of airglow depletions.
4. The altitude–latitude limits of the ESF instability processes obtained by geomagnetic field line 'apex mapping' of the airglow depletions.
5. Thermospheric dynamics associated with the midnight temperature maximum (MTM), as derived from a 'brightness wave' that passes through the field of view.

INSTRUMENTATION

The imaging system constructed for deployment in Arequipa was essentially a copy of the CEDAR Class-1 system installed in the Boston University optical building at the Haystack/Millstone Hill ISR observatory (Fig. 2). Our approach to wide field imaging science, both in 2-dimensinal imagers and for imaging spectrographs, is described in Baumgardner *et al.* (1993). For the site at Arequipa, the telephone service is not yet sufficiently reliable to use the 'telescience' subsystem shown in Fig. 2, but all other aspects are essentially identical. Images are taken at multiple wavelengths at multiple exposures and repetition rates from about an hour after sunset to an hour before sunrise, for 14 days per month centered on the date of new Moon. The imager runs in a fully automated mode for up to a year using an ephemeris of start/stop times and a pre-selected menu of observing modes; the latter can be adjusted in realtime when reliable telephone service is available. The routine set of filters used includes oxygen emissions at 5577 Å, 6300 Å, and 7774 Å, with an off-band/control image at 6644 Å used for photometric calibration of the 6300 Å images. Observations are written to one side of an optical disk each month, and the data are mailed back to Boston for analysis and archiving at bimonthly intervals.

RESULTS

Morphological patterns

Figure 3 gives the distribution of meteorological conditions and airglow events observed for the first 18 months of operation. Perhaps first to note is the reliable nature of a relatively simple and robust instrument; data were obtained during each month of the year. Except for the solstice period from November to February, there are more clear than cloudy nights for two thirds of the year. The occurrence of north–south aligned airglow depletions associated with equatorial spread-*F* (ESF) activity tends to peak in equinox months, consistent with long recognized seasonal–longitude patterns for ESF (Maruyama and Matuura, 1984; Tsunoda, 1985; Aarons, 1993). The 'brightness wave' feature (to be described below) was most prominent in the two October periods, with little or no occurrence during the December solstice periods.

Figure 4 gives an example of all-sky images at three wavelengths obtained on the night of 12 October 1993. Weak background airglow appear in all three oxygen emissions, as do bands of depletions running north to south, and drifting eastward. While the airglow signatures of depleted fluxtubes associated with ESF plumes at the equator have been described using both 6300 Å images (Weber *et al.*, 1978; Mendillo and Baumgardner, 1982; Malcolm *et al.*, 1984) and 7774 Å images (Moore and Weber, 1981; Tinsley, 1982; Mendillo *et al.*, 1985; Rohrbaugh *et al.*, 1989; Tinsley *et al.*, in press), we believe the results in panel (a) to be the first published example of such patterns in 5577 Å images. The 6300 Å and 7774 Å emissions arise from *F*-region plasma loss processes (Tinsley and Bittencourt, 1975; Bittencourt *et al.*, 1983) that are relatively uncontaminated by mesospheric sources, such as OH emissions. At 5577 Å, the low altitude mesospheric sources can be dominant, and thus the small variations in total brightness needed to define *F*-region plasma structures can be quite small, but detectable (Fagundes *et al.*, 1995a). Since the F-region 5577 Å and 6300 Å come from the same O_2^+ dissociative recombination loss process, these are expected to show very similar structures, as is indeed the case in panels (a) and (b). When mesospheric brightness levels dominate total emission, neutral atmospheric gravity wave signatures can be detected (Fagundes *et al.*, 1995b) as described below.

The 7774 Å line is a very weak emission from the direct radiative recombination of O^+ and e^-, and thus comes from higher portions of the *F*-region than the thermospheric induced 6300 Å. For example, while 6300 Å peak volume emission rates usually fall between 250 km and 350 km, at 7774 Å the altitude of peak emission is more closely linked to N_{max} at h_{max}, and thus can be rather high (>400 km) during post sunset hours near the equator (Mendillo *et al.*, 1985). The 7774 Å emission is prompt in comparison to the $\approx$120 second lifetime of the $O(^1D)$ state that gives

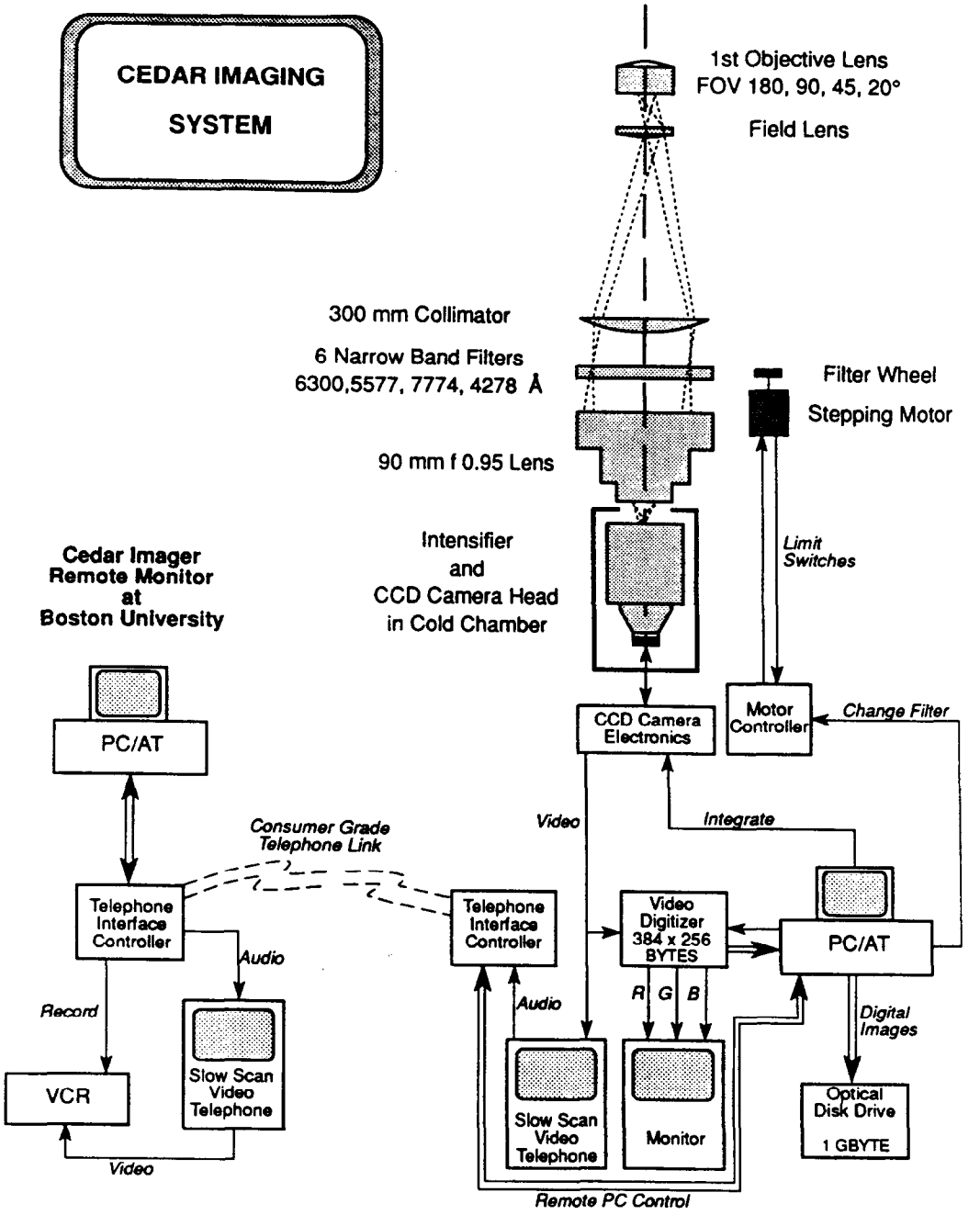

Fig. 2. Schematic of the CEDAR Class-1 imaging system as configured for remote-control, fully automated operation.

rise to 6300 Å. Thus, diffusion of the excited species (leading to less well define depletion structures) does not occur, as is nicely illustrated by Tinsley *et al.* (in press). However, background brightness levels of 7774 Å images are very low during non-solar-maximum years, and thus contrast between background and depletion structures can be quite a problem. At 5577 Å, the emission is also prompt, but its *F*-region brightness is less than at 6300 Å, and thus contrast issues persist (even without mesospheric con-

tamination). For all of these reasons, 6300 Å emission remains the wavelength of choice for most equatorial *F*-region thermosphere–ionosphere studies.

Gravity waves

On nights when *F*-region airglow depletion structures do not dominate an image, we have searched for subtle airglow signatures of gravity wave activity. Due to the low contrast of such features in our imaging system, this has not been an activity successful enough to include in the survey chart shown in Fig. 2. *F*-region gravity wave airglow signatures were successfully imaged at Arecibo for the first time just recently (Nottingham *et al.*, 1994; Miller *et al.*, 1994), while mesospheric observations have been successful at a variety of sites (Taylor *et al.*, 1987, 1991; Fagundes *et al.*, 1995b). A sequence of 5577 Å images taken at Arequipa on the night of 16 October 1993 suggested wave structures, but at a contrast level difficult to portray in individual images. An example is given in Fig. 5. A portion of the full image is displayed that corresponds to a region of ≈90 km north-to-south by ≈90 km west-to-east, for an OI 5577 Å mean emission height of 100 km. The brightness patterns were averaged along the north–south direction to yield the relative values given. The east–west pattern shows a wavelength of approximately 25 km, typical of mesospheric gravity wave effects recorded optically at off-equatorial sites (e.g. by Taylor *et al.*, 1991). This sample dataset offers promise for a systematic search for gravity wave activity in the equatorial mesosphere and thermosphere, and their possible relationship to variability in equatorial spread-*F* (ESF) onset effects.

Plasma drifts

The airglow depletions visible at each wavelength in Fig. 4 show eastward motions throughout the night. Since the reduced airglow brightness is due to reduced ionospheric chemical recombinations in the low density flux tubes that contain the ESF producing irregularities, the airglow depletions drift with the background plasma. At equatorial latitudes, post-sunset electrodynamics is a fairly well understood process (Kelley, 1989). Eastward thermospheric winds set *F*-region plasma in motion eastward via the so-called *F*-region dynamo (Rishbeth and Garriott, 1969). Thus the background plasma, airglow depletions, and ESF irregularities all drift with essentially the same zonal speed, though it may be altitude dependent. To obtain estimates of this speed from imaging data, we first scan the optical images east–west (through zenith) to obtain a cross-section of the brightness pattern for each depletion; then these cross-sectional scans are subjected to a correlation analysis leading to the best fit spatial shifts required to match the time between images. A succession of such space and time shifts leads to a drift versus local time curve for each airglow depletion. These, in turn, are averaged to yield a drift pattern for each night that has airglow depletions.

Figure 6(a) illustrates this technique using the data set illustrated (in part) in Fig. 4. Plasma drifts were computed independently for each wavelength. While there are no differences in the 5577 Å and 6300 Å results (as expected from *F*-region loss at the same altitude that produces O(^{1}S) and O(^{1}D)), there is a slighly lower speed for the 7774 Å results that come from higher *F*-region altitudes (see panel (b)). This implies a small altitude dependence of drifts over the ≈250 to ≈400 km altitudes spanned by 5577 Å, 6300 Å and 7774 Å emission processes, at least on this night. Figure 6(c) illustrates the results using 6300 Å data from 22:00 LT to 2:30 LT over a six day period in October 1993, during the so-called 'MISETA pilot' campaign that comprised the field test of the imaging system. The resultant drifts are very consistent from night-to-night, and with the Fejer (1991) drift model, also shown in panel (c). The one exception occurred on the early morning hours of 13 October when a surge in eastward drift occurred. This may have been due to penetration of substorm electric fields, or to a surge in thermospheric winds. The multi-instrument goals of the MISETA program were created to examine such issues; unfortunately, the FPI, spaced receiver and ISR were not yet in full operation during our pilot studies. A companion series of papers using all MISETA instruments during the MISETA-1 campaign of September–October 1994 has appeared (e.g., see Colerico *et al.*, 1996).

Apex mapping.

Depletions in 6300 Å emission patterns result from low plasma densities at the ionospheric heights where thermospheric O_2 produces airglow (i.e. between 250–350 km). Given the flux tube nature of the ESF instabilities processes (Haerendel *et al.*, 1992), a low plasma density at the base of a flux tube implies low densities throughout the entire flux tube. A north–south airglow depletion thus arises from the feet of many neighboring flux tubes along a geomagnetic meridian, spanning the equator, that have experienced the ESF instability. The poleward end of an airglow depletion gives the latitude extent of the ESF process for that event. The altitude crossed at the geomagnetic equator for a field line at a given latitude is called its apex heights. Thus, an image of airglow depletions (as in Fig. 4(b)) covering latitude and longitude at ≈300 km

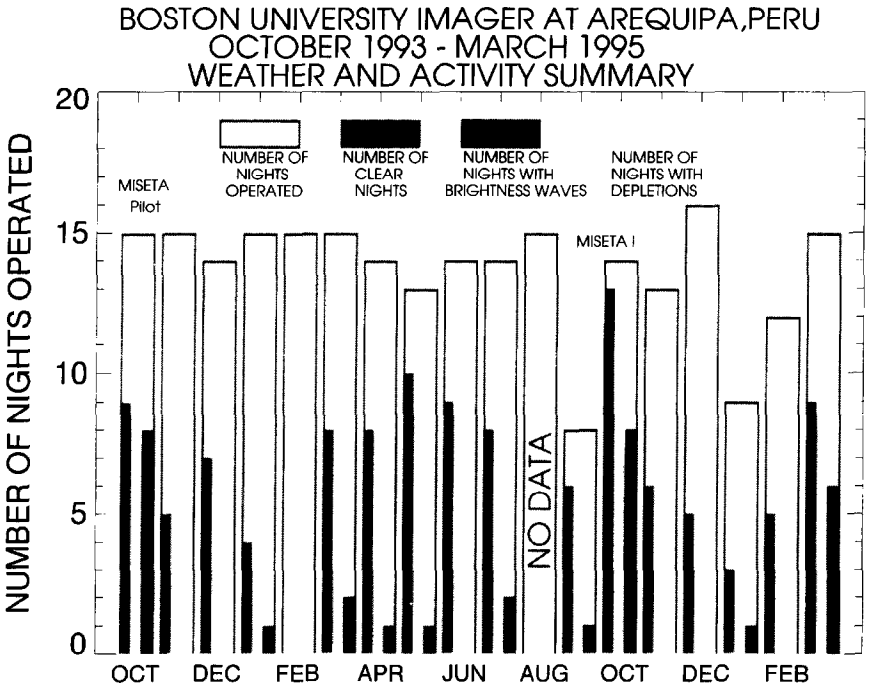

Fig. 3. Operational summary for the initial 18 months of the MISETA Imaging Science Program in Arequipa, Peru. Observations from one month (August 1993) were ultimately lost due to a failure of the optical disk writer.

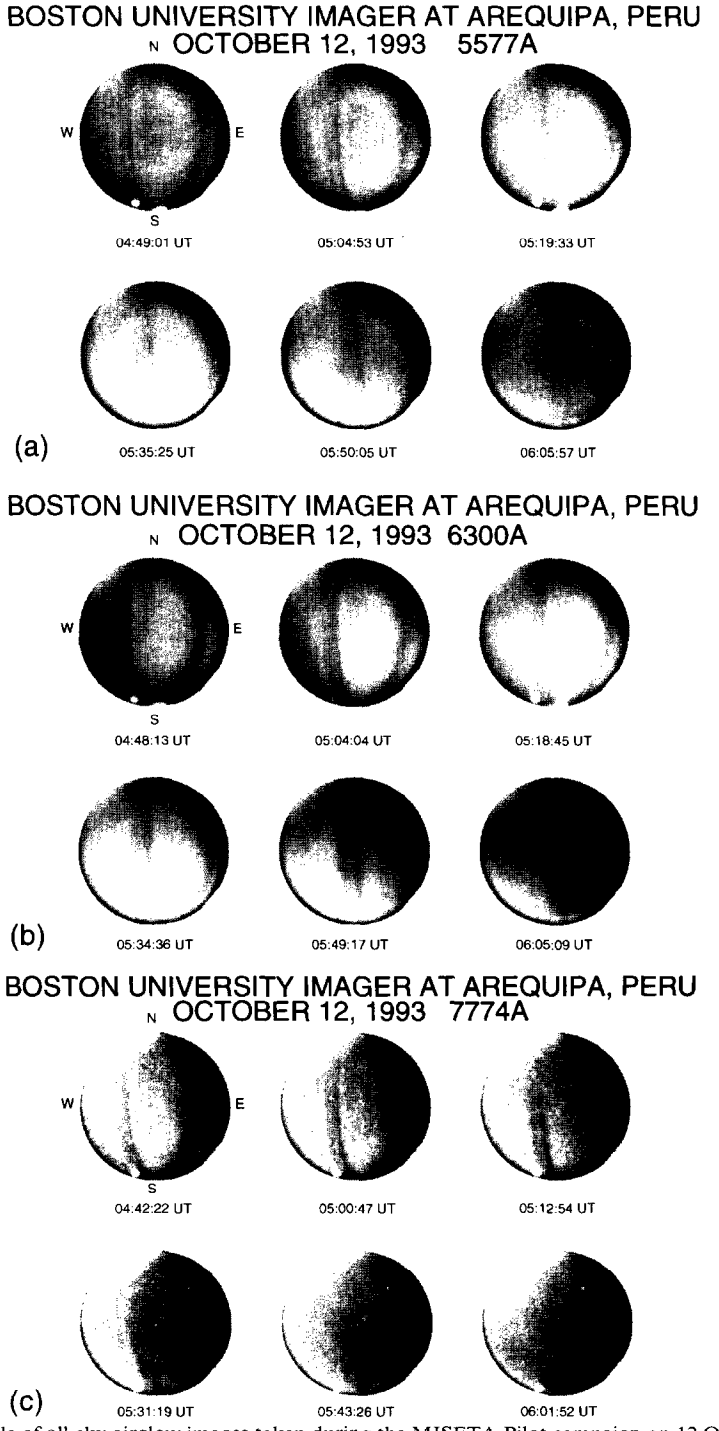

Fig. 4. Example of all-sky airglow images taken during the MISETA Pilot campaign on 12 October 1993. Panel (a) gives images in 5577 Å; (b) in 6300 Å and (c) in 7774 Å emission from neutral atomic oxygen (OI). Features to note are the north–south aligned airglow depletions in all three wavelengths, and the brightness wave that propagates towards the south-west in 5577 Å and 6300 Å, but not in 7774 Å. Depletion widths are typically 50–200 km in east–west distance (see Fig. 6a). Note that the long exposure time needed for the faint 7774 Å emission (40 s) in comparison to those for the 5577 Å and 6300 Å (6 s) accentuates the interference from the city lights of Arequipa in the north-west portion of each image.

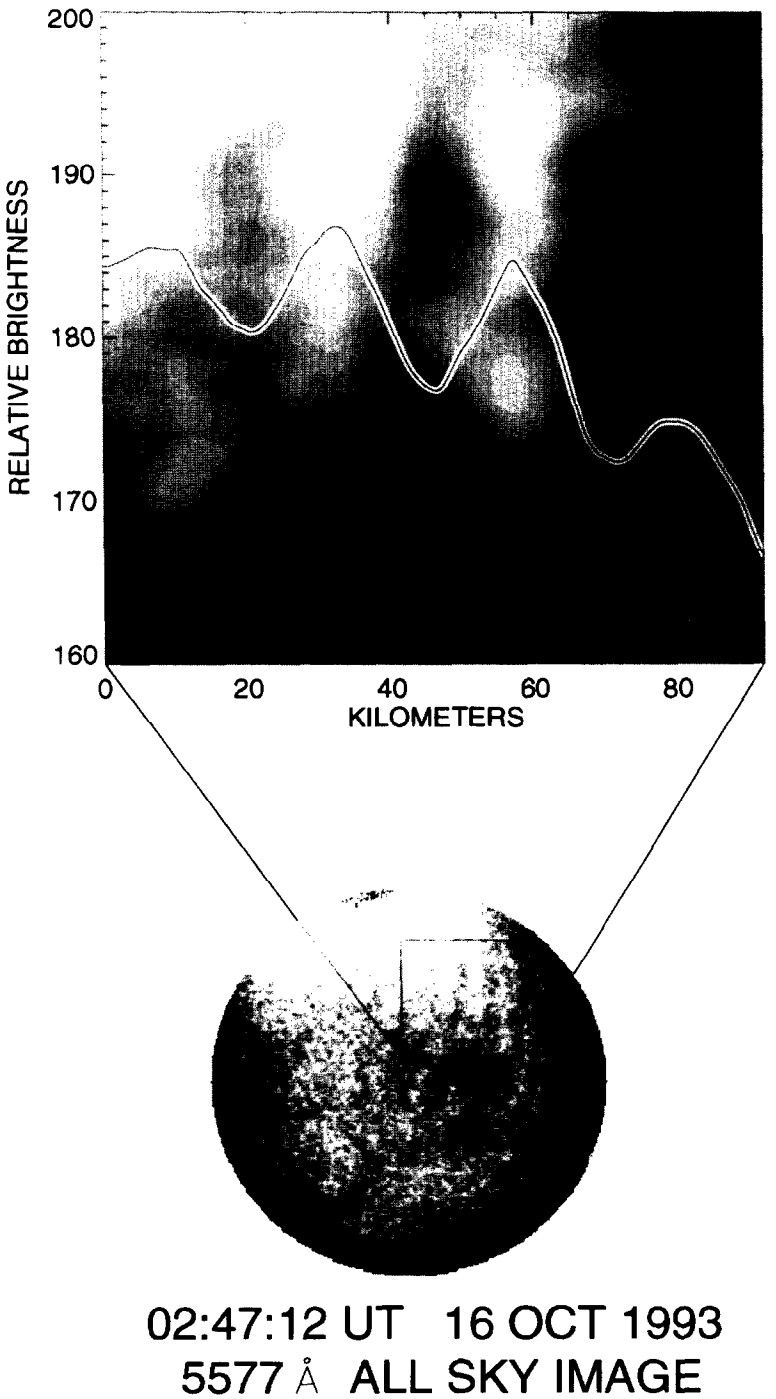

Fig. 5. Example of gravity wave activity as captured in 5577 Å images. The expanded view of a portion of the image demonstrates how subtle brightness signatures can be extracted for qualitative analysis (see test).

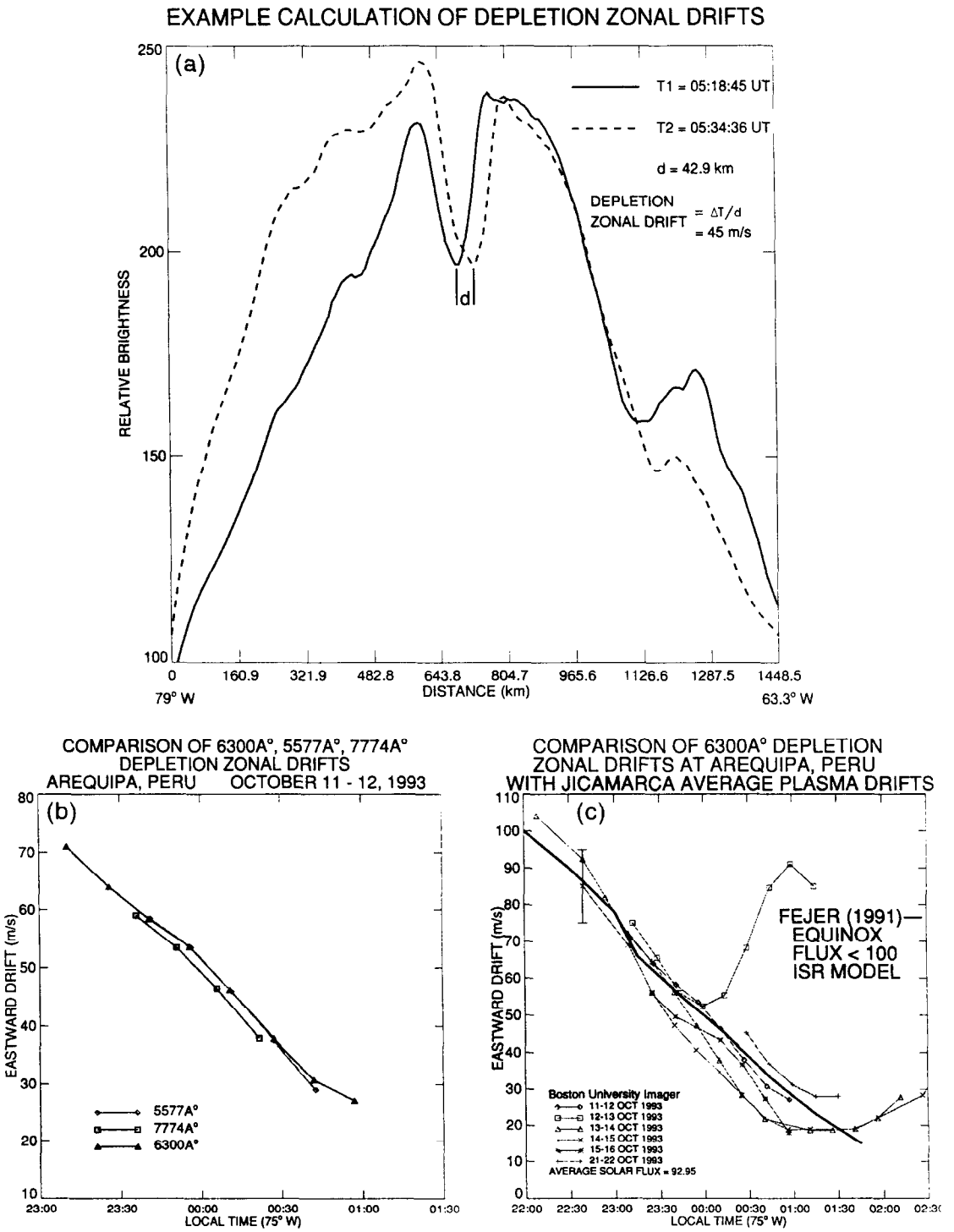

Fig. 6. (a) Example of plasma zonal drift determination using 6300 Å airglow depletion patterns. (b) Comparison of zonal plasma drifts obtained from airglow depletion motion as recorded in 5577 Å, 6300 Å and 7774 Å observations using images from the night of 12 October 1993 (see Fig. 4). (c) Examples of zonal plasma drift speeds derived from the eastward motion of airglow depletions observed in 6300 Å from six nights in October 1993. Also shown is a comparison of averaged observed zonal plasma drifts from the Jicamarca radar method under comparable conditions.

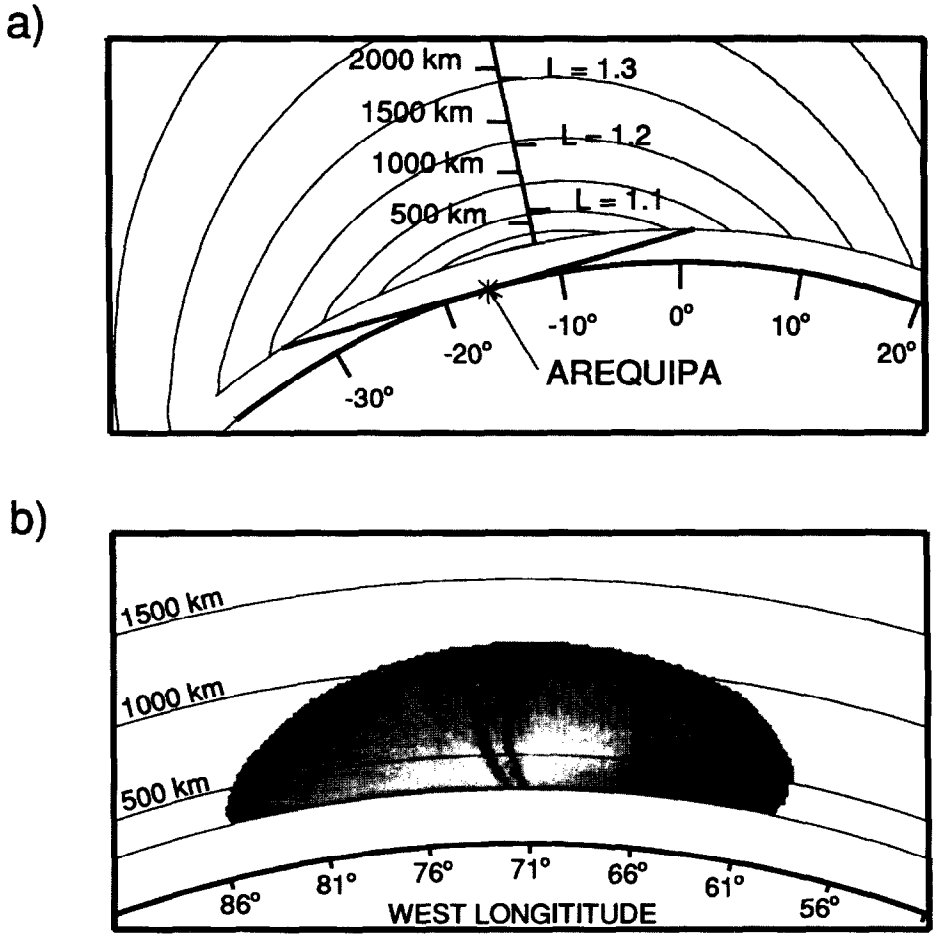

Fig. 7. Example of geomagnetic field aligned mapping of airglow depletions to the geomagnetic equator altitude–longitude plane. In panel (a), field lines to the south of Arequipa are seen to map to apex heights up to $L = 1.2$ (~ 1200 km above the geomagnetic equator). In panel (b), the portion of the image at 05:34:36 UT in Fig. 4(b) that covers regions south of the geomagnetic equator is mapped to the geomagnetic equatorial plane. All three depletions are tilted to the west of their local vertical at 300 km.

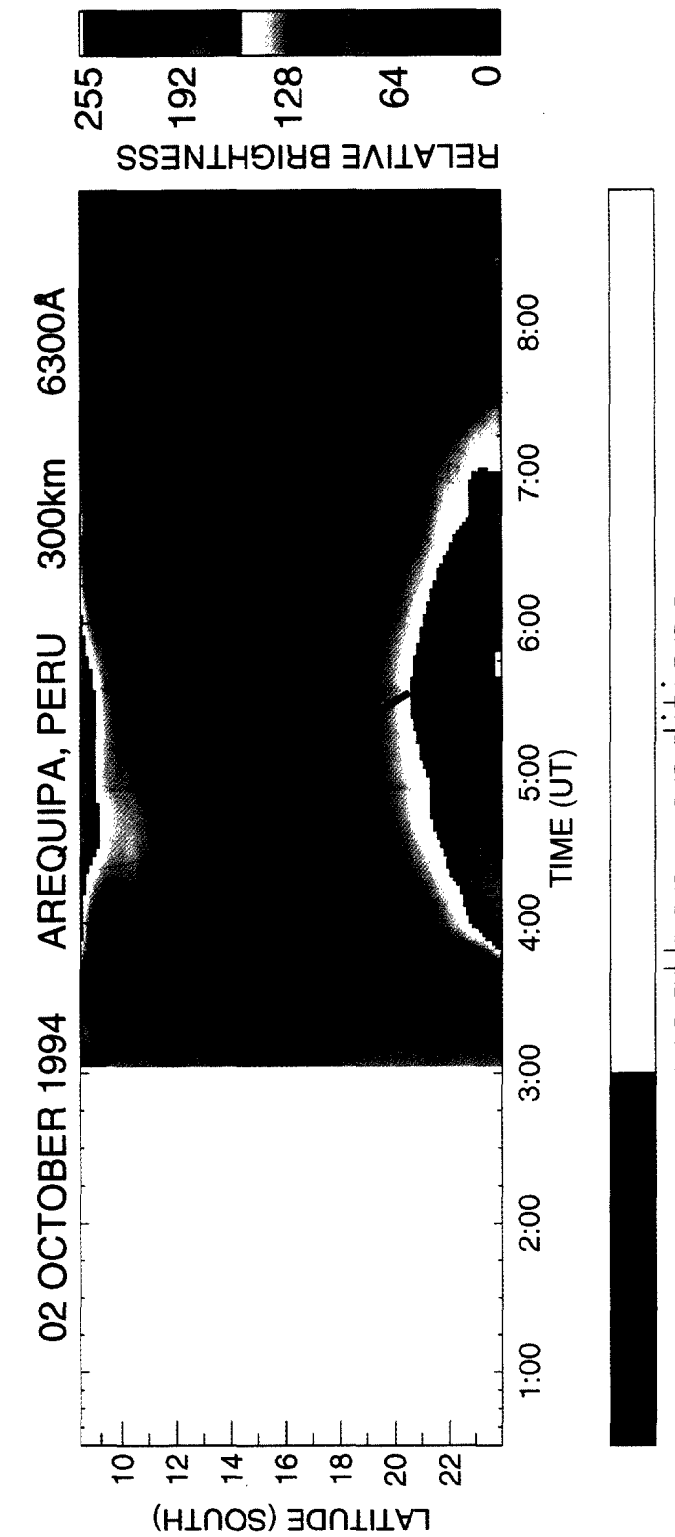

Fig. 8. Example of 6300 Å 'brightness wave' morphology using north–south scans of images (as depicted in Fig. 4b) vs time on 12 October 1993. The 6300 Å brightness values are assigned latitudes using an airglow emission height of 300 km. The slope of the line of maximum brightness gives an effective north–south wave speed components of 278 ± 12 m/s. In order to avoid using brightness signatures at the edges of the field of view, the linear fit to the peak brightness pattern was done between zenith angle of ±60°, corresponding to latitudes of ~12° S to ~20° S.

can be mapped along field lines to create an altitude–longitude map of ESF plumes (Mendillo and Baumgardner, 1982; Rohrbaugh *et al.*, 1989). An example of such apex mapping (using the IGRF model) is given in Fig. 7. Given the proximity of Arequipa to the geomagnetic equator, 6300 Å airglow depletions extending to the southern edge of the field of view map to ≈ 1200 km above the equator. Airglow depletion apex maps from Arequipa can be used to study onset and growth patterns for ESF effects over the same altitude range usually covered when the Jicamarca ISR is in operation (a few days/month); imaging observations taken more frequently can thus contribute to such datasets. Finally, tilts in the mapped depletions can be related to altitude dependent plasma drifts (Mendillo and Tyler, 1983), and these, in turn, to latitude dependent zonal winds (Anderson and Mendillo, 1983). As shown in Fig. 6(b), the slight decrease in plasma drift with altitude on this night is consistent with the occurrence of tilted depletions.

Midnight temperature maximum.

An anomaly associated with the thermal behavior of the upper atmosphere resulted in an unexpected observation of a transient airglow structure recorded by the MISETA imager in Arequipa. This is shown in Fig. 4 (a and b) as the region of 5577 Å and 6300 Å brightness that appears first slightly to the northeast of zenith, then fills the zenith area of the field-of-view (FOV), and finally exits towards the southwest. The map in Fig. 1 shows that the northern areas of the FOV are at or near the geomagnetic equator; wind induced vertical motions in those portions of the FOV would be very small and thus any airglow signatures they produce (as will be argued below) are not very bright. Thus, while a rapid run 'movie' of image sequences shows a propagating effect, the images displayed capture only its exit from zenith. Events as shown in Fig. 4 (a and b) occurred within a few hours of midnight on 8 of 9 clear nights that comprised the MISETA-pilot campaign. As shown in Fig. 4 (c) this feature is not apparent in the 7774 Å images. This suggest that the pattern arises from downward plasma motions into regions of enhanced chemical loss for emission mechanisms that depend on the abundance of thermospheric O_2. This is not the case for direct radiative recombination emissions from O^+ and e^- (7774 Å) that peak at h_{max}, (i.e. from a mechanism that is insensitive to $N_e(h)$ re-distributions).

The 'brightness wave' described above is better defined in north–south scans of all 6300 Å images during an evening. These latitudinal slices are stacked in chronological order resulting in a latitude vs time plot that is similar to that obtained from meridional photometer scans, except that all zenith angles are observed at the same time in an image. The $\pm 75^\circ$ zenith angle coverage results in latitudes at 300 km from 8° to 23°S. Using only zenith angles $< \pm 60^\circ$ to avoid edge effects, the temporal maxima at each degree of latitude were fitted to a straight line in latitude and time to yield the north-to-south phase speed (V_{NS}). The results of such an analysis for 12 October 1993 are given in Fig. 8. For this case, an apparent polward speed of $278 \pm 12\,m\,s^{-1}$ was obtained; the average V_{NS} from all 8 nights of observation was $300 \pm 31\,m\,s^{-1}$.

Our preliminary conclusion is that the brightness wave results from airglow produced by poleward winds generated by the so-called midnight temperature maximum (MTM), as described by Herrero and Spencer (1982). As the MISETA imager approaches this MTM region (fixed in local time), the rapid motion of the brightness wave is derived from the co-rotation speed (V_{CO}), the apparent meridional speed (V_{NS}), and the westward azimuth (θ) of the MTM pattern via $\tan(\theta) = V_{CO}/V_{NS}$. At Arequipa's latitude ($\approx 16^\circ$S), V_{CO} is approximately $445\,m\,sec^{-1}$, which yields $V_{NS} = 300\,m\,sec^{-1}$ when $\theta = 56^\circ$. Thus, the MTM zone of poleward winds is tilted (on average) westward by $\approx 56^\circ$ from the north–south meridian. Imager results as portrayed here will be able to describe MTM generated effects in a two-dimensional format. This should help in our attempts to understand the tidal interactions that cause the MTM (Fesen, 1997) and perhaps in their day-to-day variability. A more complete treatment of the optical signatures of MTM pressure bulge phenomena, as encountered by the imager in Arequipa during both MISETA campaigns (October 1993 and 1994), is presented by Colerico *et al.*, 1996.

SUMMARY

The MISETA imager is the first CCD-based all-sky airglow imaging system to operate on a continuous basis from an equatorial site with multi-diagnostic capabilities, including an incoherent scatter radar and a Fabry–Perot interferometer. Previous campaign-based imagers for ESF related studies have operated for limited durations in the Ascension Island, Peruvian, Hawaiian, and Kwajalein sectors. A 35 mm film-based imager has operated at equatorial anomaly latitudes in Brazil, with a significant yield of results during geomagnetically quiet and disturbed periods (Sahai *et al.*, 1994). New CCD imagers have recently been

installed in India (Mukherjee *et al.*, 1993; Sridharan, 1995) and a campaign mode instrument now exists in Japan (S. Fukao, private communication, 1995). The pioneering technique introduced by Weber *et al.* (1978) has thus generated an international community of observers that use the all-sky imaging mode to study equatorial aeronomy, primarily linked to ESF related phenomena. In this paper, we have reviewed the scientific yield from such observations, and demonstrated how the technique can be used to study additional aspects of ionospheric–thermospheric coupling in the equatorial region. These include extension of the technique to mesospheric gravity wave and midnight temperature anomaly effects upon the upper atmospheric system.

Acknowledgements—This work is supported, in part, by the US/NSF program in Aeronomy through Grant ATM-9204013 and by the Office of Naval Research through Grant N00014-93-0786. We are grateful for valuable discussion with the MISETA PI, Dr J. Meriwether, and for the assistance with the installation and maintenance of the MISETA imager provided by D. Hallenbeck of the NASA Tracking Station in Arequipa, Peru.

REFERENCES

Aarons J. 1993 The longitudinal morphology of equatorial *F*-layer irregularities relevant to their occurrence. *Space Sci. Rev.* **63**, 209–243.

Anderson D. N. and Mendillo M. 1983 Ionospheric conditions affecting the evolution of equatorial plasma depletions. *Geophys. Res. Lett.* **10**, 541–544.

Baumgardner J., Flynn B. and Mendillo M. 1993 Monochromatic imaging instrumentation for applications in aeronomy of the Earth and planets. *Optical Eng.* **32**, 3028–3032.

Bittencourt J. A., Teixeira N. R., Sahai Y. and Takahashi H. 1983 Mapping of ionospheric *F*-region parameters from atomic oxygen airglow emissions. *J. atmos. terr. Phys.* **45**, 697–705.

Colerico M., Mendillo M., Nottingham D., Baumgardner J., Meriwether J., Mirick M., Reinish B., Scali J. and Fesen C. 1996 Coordinated Measurements of *F*-region dynamics related to the thermospheric midnight temperature region. *J. Geophys. Res.* **101**, 26783–26793.

Fagundes P. R., Sahai Y. and Takahashi H. 1995a Investigation of OI 557.7 nm and OI 630.0 nm nightglow intensity ratios during the occurrence of equatorial *F*-region plasma bubbles. *J. atmos. terr. Phys.* **57**, 929–932.

Fagundes P. R., Takahashi H., Sahai Y. and Gobbi D. 1995b Observations of gravity waves from multispectral mesospheric nightglow emission observed at 23°S. *J. atmos. terr. Phys.* **57**, 395–405.

Fejer B. G. 1991 Altitude electrodynamic plasma drifts: A review. *J. atmos. terr. Phys.* **53**, 677–693.

Fesen C. C. 1997 Simulations of the low latitude midnight temperature maximum. *J. atmos. terr. Phys.*, (*this issue*).

Haerendel G., Eccles J. V. and Cakir S. 1992 Theory of modeling the equatorial evening ionosphere and the origin of the shear in the horizontal plasma flow. *J. geophys. Res.* **97**, 1209–1223.

Herrero F. A. and Spencer N. W. 1982 On the horizontal distribution of the equatorial thermospheric midnight temperature maximum and its seasonal variation. *Geophys. Res. Lett.* **9**, 1179–1182.

Kelley M. C. 1989 *The Earth's Atmosphere*, Chapter 3. Academic Press, Inc., Harcourt Brace Jovanovich, San Diego.

Malcolm R., Miles C. and Tinsley B. A. 1984 Field-aligned observations of trans-equatorial bubbles from Rarotonga in 1969–70. *Geophys. Res. Lett.* **11**, 665–668.

Maruyama T. and Matuura N. 1984 Longitudinal variability of annual changes in activity of equatorial spread *F* and plasma bubbles. *J. geophys. Res.* **89**, 10,903–10,912.

Mendillo M. and Baumgardner J. 1982 Airglow characteristics of equatorial plasma depletions. *J. geophys. Res.* **87**, 7641–7652.

Mendillo M. and Tyler A. 1983 The geometry of depleted plasma regions in the equatorial ionosphere. *J. geophys. Res.* **88**, 5778–5782.

Mendillo M., Spence H. and Zalesak S. T. 1985 Simulation studies of ionospheric airglow signatures of plasma depletions at the equator. *J. atmos. terr. Phys.* **47**, 885–893.

Miller C., Mendillo M., Swartz W. and Kelley M. 1994 Observations of gravity-wave induced ionospheric electric fields at mid-latitudes. *EOS* 489.

Moore J. G. and Weber E. J. 1981 OI 6300 and 7774 Å airglow measurements of equatorial plasma depletions. *J. atmos. terr. Phys.* **43**, 851–858.

Mukherjee G. K., Carlo L. and Patil P. T. 1993 First all sky imaging observations from India, South Pacific STEP Workshop, University of Newcastle, Newcastle, Australia, July 5–9, 1993.

Nottingham D., Mendillo M., Baumgardner J. and Kelley M. 1994 6300 Å airglow wave structure from Aercibo in January 1993, *EOS* 488.

Rishbeth H. and Garriott O. K. 1969 *Introduction to Ionospheric Physics*, Chapter 7. Academic Press, New York.

Rohrbaugh R. P., Hansen W. B., Tinsley B. A., Cragin B. L. and McClure J. P. 1989 Images of transequatorial bubbles based on field-aligned airglow observations from Haleakala in 1984–1986. *J. geophys. Res.* **94**, 6763–6770.

Sahai Y., Aarons J., Mendillo M., Baumgardner J., Bittencourt J. A. and Takahashi H. 1994 OI 6300 nm imaging observations of equatorial plasma depletions at 16°S dip latitude. *J. atmos. terr. Phys.* **56**, 1461–1475.

Sridharan R. 1995 Optical studies of the equatorial ionosphere–thermosphere system, IUGG XXI General Assembly, Boulder, Colorado, July 2–14, 1995.

Taylor M. J. Hapgood M. A. and Rothwell P. 1987 Observations of gravity wave propagation in the OI (557.7 nm), Na (589.2 nm) and the near infra-red OH nightglow emission. *Planet. Space Sci.* **35**, 413–427.

Taylor, M. J., Espy P. J., Baker D. J., Sica R. L., Neal P. C. and Pendleton Jr, W. 1991 Simultaneous temperature and imaging measurements of short period wave structure in the OH nightglow emission. *Planet. Space Sci.* **39**, 1171–1188.

Tinsley B. A. 1982 Field aligned observations of transequatorial bubbles in the tropical *F*-region. *J. atmos. terr. Phys.* **44**, 547–557.

Tinsley B. A. and Bittencourt J. A. 1975 Determination of *F*-region height and peak electron density at night using airglow emissions from atomic oxygen. *J. geophys. Res.* **80**, 2333–2337.

Tinsley B. A., Rohrbaugh R. P., Hanson W. B. and Broadfoot A. L. 1997 Images of trans-equatorial *F*-region bubbles in 630 and 777 nm emission compared with satellite measurements. *J. geophys. Res.*, (*in press*).

Tsunoda R. T. 1985 Control of the seasonal and longitudinal occurrence of equatorial scintillations by the longitudinal gradient in integrated *E*-region Pedersen conductivity. *J. geophys. Res.* **90**, 447–456.

Weber E. J., Buchau J., Eather R. and Mende S. B. 1978 North–south aligned equatorial airglow depletions. *J. geophys. Res.* **83**, 712–716.